Available online at www.sciencedirect.com

SciVerse ScienceDirect

Ceramics International 38 (2012) 3569–3582

CERAMICS INTERNATIONAL

www.elsevier.com/locate/ceramint

Comparative study of hydroxyapatite/gelatin composites reinforced with bio-inert ceramic particles

C. Kailasanathan [a], N. Selvakumar [b,*]

[a] Department of Mechanical Engineering, Sethu Institute of Technology, Pulloor, Kariapatti 626 115, Virudunagar District, Tamilnadu, India[1]
[b] Department of Mechanical Engineering, Mepco Schlenk Engineering College, Sivakasi, Tamilnadu 626 005, India

Received 11 October 2011; received in revised form 14 December 2011; accepted 27 December 2011
Available online 4 January 2012

Abstract

Recently, nano bio-composites have emerged as an efficient strategy to upgrade the structural and functional properties of synthetic bone grafts. Bioinert ceramics have attracted wide attention because of their biocompatibility. Novel composites of nano-hydroxyapatite/GEL with incorporation of bioinert ceramics like Al_2O_3, TiO_2 and ZrO_2 for different composites as a reinforcing phase to increase its mechanical properties was prepared. The nHAp with the size of 10–50 nm in diameter and 50–100 nm in length was uniformly distributed into GEL matrix to form the composite. It was found that the composite with a high ceramic content has good homogeneity and mechanical strength, which are close to the cancellous bone. An interconnected porous material with porosity of at least 74% was achieved by phase inversion method. The formation reaction of the nHAp/GEL/bioinert ceramic nanocomposite was then investigated via FT-IR, XRD, TG/DTA and SEM. The organic–inorganic interaction between HAp nano crystallites and GEL molecules were confirmed from FT-IR and TG/DTA. The compressive strength of bioinert ceramic reinforced nanocomposites scaffolds could high up to 13.15 MPa while those of nHAp/GEL were 4.87 MPa. The nano indentation technique was used to find nano hardness and fracture toughness was evaluated by Vickers indentation.

Keywords: Nano bio-composite; Hydroxyapatite; Nano hardness; Bio-ceramic

1. Introduction

The field of nanocomposite materials has held the attention, imagination, and close scrutiny of scientists and engineers in recent years. This scrutiny results from the simple premise that using building blocks with dimensions in the nano size range makes it possible to design and create new materials with unprecedented flexibility and with improvement in their physical properties. The concept of enhancing properties and improving the characteristics of materials through the creation of multiple-phase nanocomposites has been practiced ever since civilization started. Bone is considered as essentially a nanocomposite of hydroxyapatite (HAp: $Ca_{10}(PO_4)_6(OH)_2$) nanocrystals and type-I collagen [1]. Chang and his workers [2,3] have developed an imitation bone using biomimetic process, which is based on the idea that biologic systems store and process information at the molecular level [4]. As an artificial bone substitute, HAp-embedded GEL nanostructure has been reproduced using a biomimetic co-precipitation reaction of HAp nanocrystals in a soluble GEL matrix. In order to give better toughness for the materials, HAp/GEL nanocomposite was cross-linked by glutaraldehyde, which has been widely used for the cross-linkage of GEL [5]. Hydroxyapatite has been intensively investigated as a bone substitute due to its similar biocompatibility and osteo conductivity to bone [6–8]. It could be natural or synthetic, and it possesses excellent biocompatibility with bones, teeth, skin, and muscles, both in vitro and in vivo. HAp promotes faster bone regeneration, and direct bonding to regenerated bones without intermediate connective tissues. It has been developed as a bone graft substitute and it is currently used in clinical applications. However, due to the brittleness of the HA and the lack of interaction with the polymer, the ceramic nanoparticles may present deleterious effects on the mechanical properties, when added at high loadings since it is of a great interest to the biomedical community.

* Corresponding author. Tel.: +91 4562 235641.
E-mail addresses: uthrakailash@yahoo.co.in (C. Kailasanathan), nsk2966@yahoo.co.in (N. Selvakumar).
[1] Tel.: +91 4566 308001.

0272-8842/$36.00
doi:10.1016/j.ceramint.2011.12.073

There have been some difficulties to attain sufficient mechanical strength and a proper pore size compared to biological bone. The properties of biological bone tissue are essentially based on the organic–inorganic interaction between calcium phosphate (Ca-P) or HAp and the protein matrix. In this report, the needle like nHAp reinforcement was modified with the addition of bioinert ceramics such as alumina, titania, zirconia and the organic–inorganic interaction between the GEL matrix and nHAp was investigated in the nHAp/GEL nanocomposite. The organic–inorganic interaction between the GEL and the ceramics greatly contributed to the formation of porous scaffolds which otherwise would facilitate cell growth and the transfer of nutrients and excretion of the waste products. Further, a single-phase material also called monolithic does not always provides all the essential features required for bone growth. Therefore, there is a great need for engineering multi-phase materials also called composite with structure and composition similar to natural bone [9,10]. It is well known that higher HAp content in the composites could achieve better bioactivity [11,12]. However, the mechanical strength of the high HAp content composites could also be directly affected by the size and dispersion properties which are differently controlled during the whole manufacturing process [13]. It has been reported that the mechanical strength of HAp/polymer composites can only be achieved when the HAp particles is small and uniformly dispersed inside the composite. Therefore, nano-apatite crystals have been used, as reinforcements for this kind of composites preparation. GEL satisfies most of the requirements of organic phase of a native bone due to its good mechanical properties, low toxicity and predictable biodegradation kinetics [9]. The flexibility and cost-effectiveness of GEL can be combined with the bioactivity and osteo conductivity of nHAp to generate potential engineering biomaterials. Bioinert ceramics are added to nHAp/GEL composite in order to obtain high fracture toughness, high porosity and excellent biocompatibility [14,15]. In the first step, needle-like nHAp particles were synthesized using wet chemical method. In the following steps, pure nHAp/GEL scaffold and scaffolds comprising different contents of nHAp, bioceramic particles in the GEL matrix were fabricated using phase inversion method. The porous scaffold generated by this method exhibited well-developed structural features.

2. Materials and methods

2.1. Chemicals

Deionized water was used in all reactions. The sodium hydroxide [NaOH] pellets were used as purchased (Merck) to prepare NaOH solution. Analytical grade of diammonium hydrogen phosphate [$(NH_4)_2HPO_4$], ethanol and calcium nitrate [Ca $(NO_3)_2{\cdot}4H_2O$] were used as supplied (Merck).

2.2. Synthesis of nHAp powder

A sol–gel auto combustion route and wet chemical method have been recommended to synthesize nano powders in order to obtain fine crystal size [15]. The nano particles prepared by electro-reduction processes [16] are formed as spongy layers that can be easily separated to give fine particles and a novel laser–liquid–solid interaction (LLSI) technique [17] is also used to prepare nano materials in the form of particles, rods, and tubes from liquid precursors. Pure and cobalt-exchanged hydroxyapatite (HAp and CoHAp) powders are synthesized by hydrothermal method [18]. In this study, the nHAp nanocrystals were synthesized by wet chemical method [19]. In this method, 0.03 M aqueous solution of diammonium hydrogen phosphate was added drop wise to 0.05 M aqueous solution of Ca $(NO_3)_2{\cdot}4H_2O$ as P and Ca precursors respectively. Before mixing, the pH value of $Ca(NO_3)_2{\cdot}4H_2O$ solution was adjusted to 11 by adding sodium hydroxide solution and the temperature was maintained at 70 ± 5 °C. The precipitated nHAp mixture was aged for 24 h at room temperature and centrifuged at the rotation speed of 9000 rpm for 0.5 h in a Remi rotor. Then the powder was frozen at −20 °C for 1 h and dried in freeze dryer system at −75 °C for 1 week and calcined at 600 °C for 1 h.

2.3. Synthesis of nHAp/GEL and nHAp/GEL/Bio inert ceramic composites

Porous objects of hydroxyapatite composites may be prepared by mixing sodium chloride as channeling agent with ultra-high molecular weight polyethylene as a binder [20]. In this work, the nHAp/GEL porous scaffold was prepared by thermally induced phase inversion [21]. A homogeneous multi component system was prepared by mixing nHAp/GEL composite powders with ethanol at room temperature (Fig. 1). To control the porosity of the resulting porous scaffolds, the composite to ethanol ratio (w:v) varied from 0.6 to 0.8. After complete mixing, the scaffold was moved into ultrasonic vibration for 15 min. Then the scaffold was moved into the oven at a temperature of 50 °C for 3 days. During this period, phase inversion of ethanol was thermally induced by changing the temperature higher than the critical temperature of ethanol, that is, ethanol in liquid phase changed into gaseous one. As time passed, the gas nuclei gradually grew bigger and bigger, and even interconnected to each other. Following this nucleation and growth mechanism, an inter connective porous structure was formed [22]. Simultaneously, ethanol gradually evaporated and it leads to the solidification of the material. After complete solidification, the porous foam was removed from the mould and ultrasonic washing in deionized water for 24 h to thoroughly eliminate the leftovers of ethanol. The porous composite scaffold was obtained after dried at 50 °C. Similarly, alumina was added to nHAp with the ratio (nHAp:alumina = 50:10, 40:20, 30:30 and 20:40) along with 40% GEL. Thus, different nHAp/GEL/Al_2O_3 composites with different weight % were prepared. In the same way, the different composites of nHAp/GEL/TiO_2 and nHAp/GEL/ZrO_2 with various weight percentages were prepared.

2.4. Characterization

2.4.1. FTIR analysis

The Fourier transform infrared (FTIR) spectra were collected for the powders using a Bruker Optics FTIR

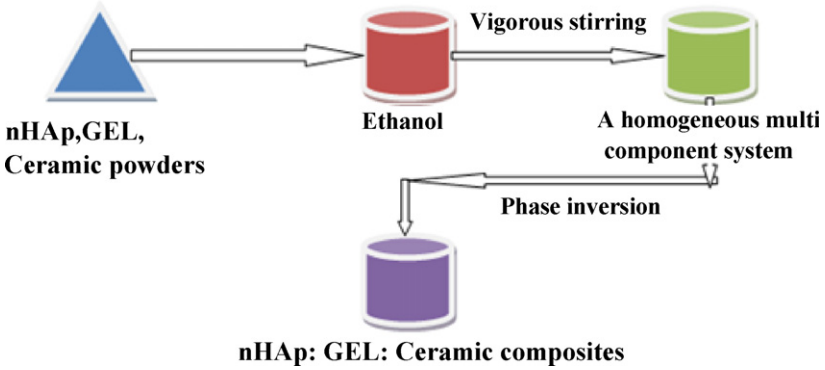

Fig. 1. Fabrication processes of nHAp:GEL:ceramic composite scaffolds using phase inversion method.

spectrometer, Germany. Spectra were obtained at 4 cm^{-1} resolution, averaging 24 numbers of scans.

2.4.2. XRD analysis

X-ray powder diffraction (XRD) patterns were obtained for the powder samples using PANalyticalX'per PRO diffractometer using Cu-Kα radiation (λ = 0.15418 nm). Data was collected over the 2θ range 10–90° with a step size of 0.0170° and step time of 15.5076 s.

2.4.3. SEM analysis

The morphology of the synthesized nHAp and composite scaffolds were observed by scanning electron microscopy (SEM, Make: Hitachi, Japan, Model: SU510). Prior to examination, each sample was ion sputtered with gold to enhance charging of particles.

2.4.4. Thermo gravimetric analysis (TG/DTA)

The powders produced by the wet chemical process were studied by TG/DTA to determine the mass variation in the sample. The sublimation temperatures of volatile substances were determined by DTA. A SDT Q600 V8.3 Build 101 Thermo Gravimetric Analyzer was used, the temperature interval was T_{room}, T, 1200 °C and the heating rate was 20 °C/min in air.

2.4.5. Porosity measurement

The porosity may be measured by a destructive gravimetric technique [23] and conventional liquid substitution method [19,24]. In liquid substitution method, ethanol was used as the displacing liquid because it penetrated easily into the pores of the scaffold, but not into the composite itself. Briefly, a sample of measured weight W was immersed in a graduated cylinder containing a known volume (v_1) of ethanol and kept for 24 h to allow the ethanol to penetrate into the pores of the scaffold. The total volume of the remaining ethanol and the ethanol-impregnated scaffolds was then recorded as v_2 by simply reading the level in the cylinder. The volume difference ($v_2 - v_1$) represents the volume of the scaffolds material. The ethanol impregnated scaffolds were then removed from the graduated cylinder and the residu

al ethanol volume was recorded as v_3. Hence the total volume (v) of the scaffolds was ($v_2 - v_3$) and by measuring the initial and final weights w_i and w_f, respectively after soaking in ethanol ($\rho_{ethanol}$ = 0.789 g/cm^3) for 24 h; then the porosity can be measured using the Eq. (1):

$$\text{Porosity} = \frac{(w_f - w_i)}{\rho_{ethanol}} \left(\frac{1}{v_2 - v_1} \right) \quad (1)$$

At least five scaffolds were tested for each sample and the average porosity reported.

2.4.6. Mechanical property

The compressive strength and modulus of the composite scaffolds were determined using a mechanical testing machine (TIRA Test-2720). According to ASTM D 5024-95 standard, cylindrical samples were prepared with diameters of 26 mm and lengths twice its diameter. The cross-head speed was set at 0.5 mm/min, and the load was applied until the specimen was failed. The compressive modulus was calculated as the slope of the initial linear portion of the load–displacement curve. The ultimate compressive strength and modulus was determined from the load–displacement curve. To check the reproducibility at least three specimens were tested for each sample.

3. Results and discussion

3.1. FT-IR spectroscopy

The functional groups of the synthesized nHAp powder, Al_2O_3, TiO_2, ZrO_2, GEL and nHAp/GEL composite scaffolds were evaluated using FT-IR as shown in Fig. 2. The corresponding wave numbers of characteristic groups of nHAp, Al_2O_3, TiO_2, ZrO_2, pure GEL, nHAp/GEL, nHAp/GEL/Al_2O_3, nHAp/GEL/TiO_2 and nHAp/GEL/ZrO_2 are listed in Table 1. FT-IR analysis in Fig. 2 shows some variations in adsorption peaks of the nHAp and GEL and the nano composites as below.

The nHAp/GEL nanocomposites are likely to have been formed by the interaction between the critically smaller size of the HAp nano crystallites and GEL molecule. It was noted that the PO_4^{3-} spectra pattern of nHAp is not much smoother (Fig. 2(a)). There was relatively strong interaction between Ca-P and the GEL matrix and there are greater amounts of organized components in the final nanocomposite of nHAp/GEL. From CO_3^{2-} bands of the nHAp/GEL, sample was less carbonated, indicating less potential for the carbonation of the nHAp

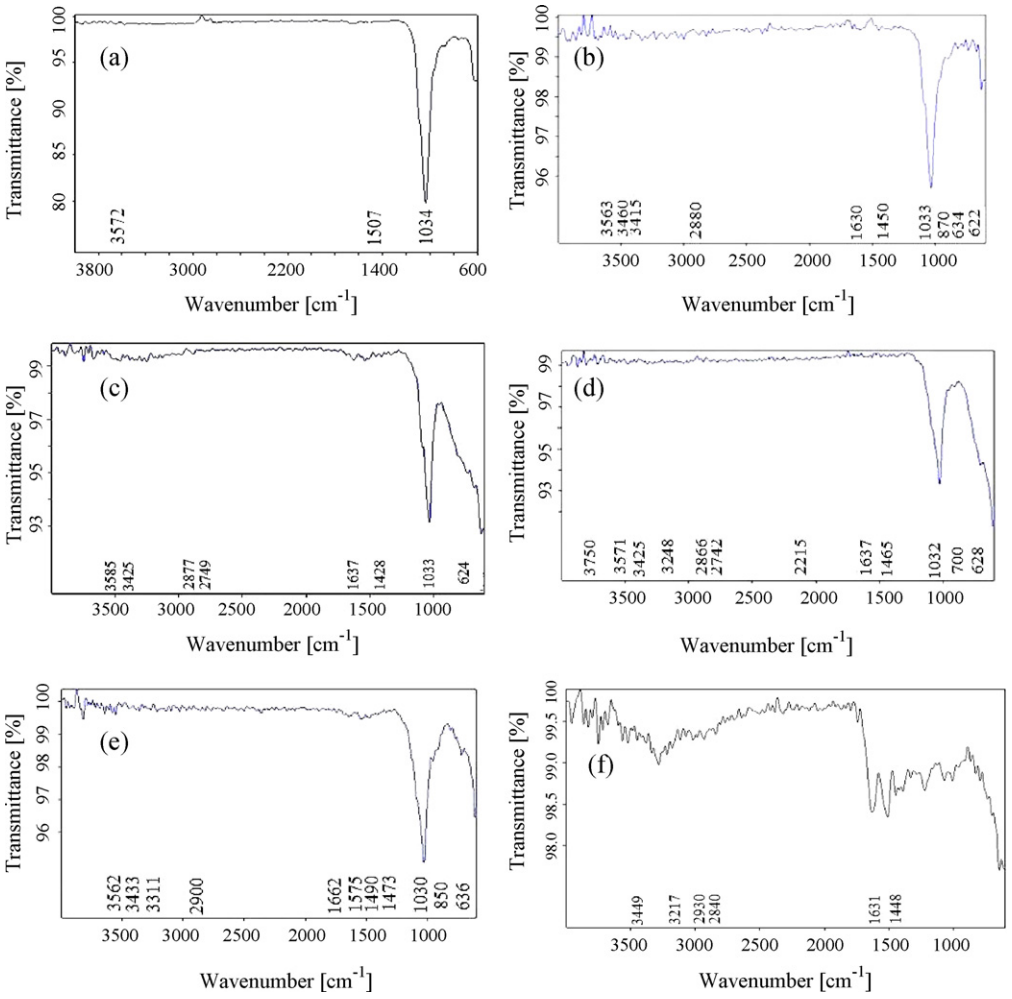

Fig. 2. FT-IR spectra of (a) nHAp, (b) nHAp/GEL, (c) nHAp/GEL/Al_2O_3, (d) nHAp/GEL/TiO_2, (e) nHAp/GEL/ZrO_2 and (f) GEL.

phase due to the highly active interaction between nHAp and the GEL matrix during the process stage. The organic–inorganic interaction was likely to be very active to formulate the nanocomposite of HAp/GEL. This was likely enhanced by the modified molecular architecture of the GEL. The spectra for the PO_4^{3-} band in nHAp/GEL indicate a greater amount of organic–inorganic interaction between HAp and the GEL (Fig. 2(b)).

PO_4^{3-} peaks of the nHAp (Fig. 2(a)) at 602, 950, 1034 and 1092 cm^{-1}, move back to 634, 954, 1033 and 1089 cm^{-1} in the nano composite (Fig. 2(b)) and to 624, 958, 1033 and 1094 cm^{-1} in the nHAp/GEL/Al_2O_3 composite (Fig. 2(c)). These peaks shift to 628, 960, 1032 cm^{-1} (Fig. 2(d)) and 1096 and to 636, 941, 1030 cm^{-1}(Fig. 2(e)) in nHAp/GEL/TiO_2 [22] and nHAp/ZrO_2, respectively. The data showed that a process of dehydroxylation and rehydroxylation might have occurred in the composite [19]. Furthermore, the wave number of–CH vibration peaks at 2930, 2840 and 2767 cm^{-1} in the GEL spectrum (Fig. 2(f), Table 1) shifted to 2880, 2821 and 2746 cm^{-1} in the nano composite (Fig. 2(b)), but reduced to 2877, 2820, 2749 cm^{-1}(Fig. 2(c)) and to 2866, 2814, 2742 cm^{-1} (Fig. 2(d)) and to 2900, 2803 cm^{-1} (Fig. 2(e)) in the nHAp/GEL/Al_2O_3, nHAp/GEL/TiO_2 and nHAp/GEL/ZrO_2 composites, respectively. These results indicate some molecular interactions between the nHAp, ceramics, and GEL matrix in the nano composites.

The –C=O vibration peak of GEL at 1631 cm^{-1}(Table 1) shifts to 1630 cm^{-1} and 1637 cm^{-1} in the nano composite nHAp/GEL (Fig. 2(b)) and nHAp/GEL/Al_2O_3 composite (Fig. 2(c)), respectively. These changes may be attributed to the formation of hydrogen bonding between –OH– group of nHAp and –C=O group of GEL in the nano composite. The intensity of –OH– absorption peaks at 3572 and 630 cm^{-1} in the nHAp (Fig. 2(a)) are decreases obviously in the nano composite. The same was observed in nHAp/GEL/Al_2O_3, nHAp/GEL/TiO_2 and nHAp/GEL/ZrO_2 –NH stretching vibrations found at 3336, 3449 cm^{-1} in the GEL spectrum are shifted to 3334, 3460 cm^{-1} in the nano composite and to 3351, 3425 cm^{-1} and to 3433, 3311 in the nHAp/GEL/Al_2O_3, and nHAp/GEL/ZrO_2, respectively [22].

The stretching vibration peak of OH– in carboxyl groups (–COOH) of GEL at 3593 cm^{-1} disappeared in all composites. It can be assumed that carboxyl groups (–COOH) of GEL were ionized to form –COO– ions during the composite formation. Al–O peak of the alumina (Table 1) at 900–950 cm^{-1} remain the same in the nHAp/Al_2O_3/GEL composite. Further, the intensity of H–O peaks at 3062–3662 cm^{-1} is shifted to 3037–3674 cm^{-1}

Table 1
Characteristic wave numbers of nHAp, Al_2O_3, TiO_2, ZrO_2, pure GEL, nHAp:GEL, nHAp:GEL:Al_2O_3, nHAp:GEL:TiO_2, nHAp:GEL:ZrO_2 [19,22].

Characteristic group	nHAp (cm^{-1})	Al_2O_3 (cm^{-1})	TiO_2 (cm^{-1})	ZrO_2 (cm^{-1})	GEL (cm^{-1})	nHAp:GEL (cm^{-1})	nHAp:GEL:Al_2O_3 (cm^{-1})	nHAp:GEL:TiO_2 (cm^{-1})	nHAp:GEL: ZrO_2 (cm^{-1})
$-PO_4^{3-}$	602	–		–	–	634	624	628	636
	950	–	–	–	–	954	958	960	941
	1034	–	–	–	–	1033	1033	1032	1030
	1092		–	–	–	1089	1094	1096	–
–OH–	630	–	–	–	–	622	630	630	620
	3572	–	–	–	–	3563	3585	3571	3562
		–	3215	–	–	–	–	3248	–
		–	3747	–	–	–	–	3750	–
		–	–	1565	–	–	–	–	1575
		–	–	3400	–	–	–	–	3433
CO_3^{2-}	873	–		–	–	870	872	875	841
	1421	–	–	–	–	1419	1428	1428	1413
	1457	–	–	–	–	1450	1453	1465	1490
Absorbed water	1631	–	–	–	–	1630	1637	1637	1662
Lattice water	3410	–	–	–	–	3415	3425	3425	3433
–C═O	–	–	–	–	1631	1635	1637	1628	1660
	–	–	2187	–	–	–	–	2190	–
	–	–	2209	–	–	–	–	2215	–
CH– stretching vibration	–	–	–	–	2767	2746	2749	2742	–
	–	–	–	–	2840	2821	2820	2814	2803
	–	–	–	–	2930	2880	2877	2866	2900
–NH stretching vibration	–	–	–	–	3336	3334	3351	–	3311
	–	–	–	–	3449	3460	3425	–	3433
–OH– in –COOH	–	–	–	–	3217–3593	Disappeared	Disappeared	Disappeared	Disappeared
$-CH_3$	–	–	–	–	1391	1352	1323	1398	–
	–	–	–	–	1448	1450	1442	1428	1473
Al-O	–	900–950	–		–	1414	900–950	–	–
H-O	–	3062–3662	–	1550	–	–	3037–3674	–	1542
Ti-O	–	–	Below 700	–	–	–	–	Below 700	–
Zr-O	–	–	–	462	–	–	–	–	–
	–	–	–	878	–	–	–	–	850

(Table 1). Similarly, H–O peak at 1550 cm^{-1} of ZrO_2 (Table 1) is also shift to 1542 cm^{-1}(Fig. 2(e)) in the nHAp/GEL/ZrO_2. These indicate that the bonding exists between nHAp, GEL and with added bioinert ceramic particles.

3.2. XRD analysis

XRD analysis results of the nHAp, nHAp/GEL composite and nHAp/bioceramic/GEL are shown in Fig. 3(a–e). The results of this study showed that the development of nHAp crystals was confirmed from XRD measurements shown in Fig. 3(a). The nHAp crystals that were synthesized revealed characteristic peaks in the XRD pattern that were consistent with JCPDS (9-0432) files for high temperature calcined nHAp [19]. Comparison of nHAp (a) with that of the composite (b and c), the peaks' position of the starting nHAp does not change in the composite. This means that the nHAp still keeps its original crystal structure in the composite. The formation and development of composite crystals was greatly influenced by the GEL during the preparation of composite. It is well known that the rate of mineral formation in bone biology is highly dependent on factors like pH and the concentration of calcium phosphate as well as other physiological ions. The only variable in this phase inversion technique of composite preparation was the ceramic content which can be correlated with the relative concentration of the physiologically important ion *x*–O–. The carboxyl ion can be an especially active site for the coordination of calcium ions to form ion complexes. These complexes can further interact with PO_4^{3-} ions due to the super saturation effects and form critical size nuclei for the nucleation and subsequent growth of composite crystals. It is noted that the nHAp sample prepared shows a good crystallinity, but the preferred (0 0 2) orientation is not readily apparent. The preferred orientation is greatly enhanced in the nHAp–GEL composite system. That is, GEL molecules in the batch induced strongly preferred development of (0 0 2) plane in nHAp crystals.

No peaks are observed for GEL since it is amorphous in structure. It can be observed in (b) and (c) that there are two characteristic peaks of alumina at $2\theta = 22^\circ$ and 49°. It can be obtained from (b) and (c) that the crystallinity of alumina in the composite is 22%. The decrease of crystallinity of alumina in composite indicates that the crystal structure of alumina changed after forming composite with nHAp, which may result from the interfacial chemical bonding formed between nHAp,

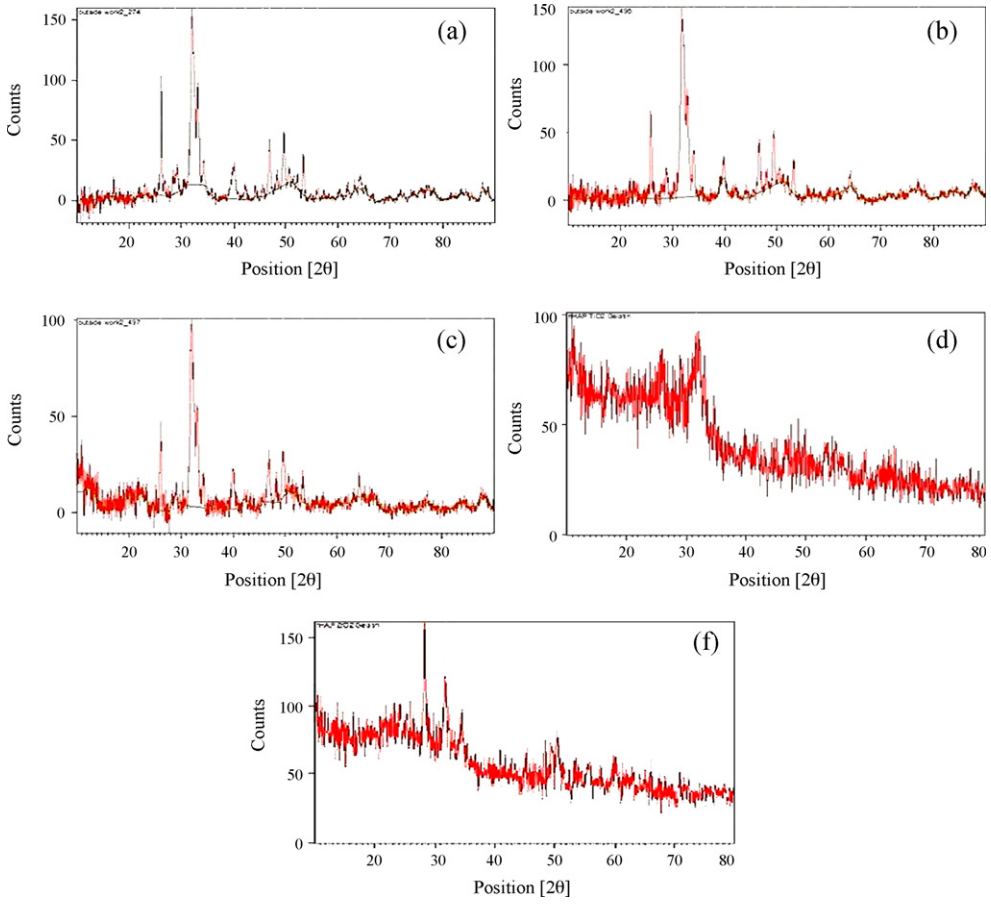

Fig. 3. XRD pattern of (a) nHAp, (b) nHAp/GEL, (c) nHAp/GEL/Al_2O_3, (d) nHAp/GEL/TiO_2 and (e) nHAp/GEL/ZrO_2.

alumina and GEL. For the nHAp/GEL/titania composite and nHAp/GEL/zirconia composite, the characteristic peaks are observed at 22°, 43° [22] and 28°, 32°, 57° respectively (Fig. 3(d and e)). The decrease of crystallinity was found in these composites also due to the formation of bonding between the inorganic and organic phases.

3.3. SEM analysis

The morphology and nanostructure of the scaffolds are examined using SEM and shown in Fig. 4. SEM micrograph of the synthesized nHAp prepared at 70 ± 5 °C with 24 h aging time is shown in Fig. 4(a). It shows needle like morphology with the particle width ranged from 100 to 175 nm and the length from 100 to 400 nm. Freeze drying has the effect of drying small sections of precipitate and gives less opportunity for particles to agglomerate. It reveals that the powder is interconnected by macro and micro-pores inside. The micro-pores in the macro-pores surface could greatly enlarge the surface contact area for protein adsorption. Hence this will enhance protein absorption on pore surface to facilitate bone formation.

The nano composite nHAp/GEL scaffold (Fig. 4(f)) maintains a regular internal ladder-like pore structure similar to pure GEL scaffold (Fig. 4(b)). Micrographs' comparison of the nanocomposite and GEL scaffolds (Fig. 4(b and f)) reveals no definite morphological differences and showed heterogeneous phases with complete fusion of nHAp crystallites into GEL matrix. Needle-like nHAp particles are distributed within the pores of the nanocomposite scaffold and no aggregation appears (Fig. 4(e and f)).

On the other hand, composites of nHAp/GEL/Al_2O_3, nHAp/GEL/TiO_2, nHAp/GEL/ZrO_2 scaffolds (Fig. 4(g–i)), ceramic particles are randomly distributed in the GEL matrix i.e. some are embedded in the pore wall and some are piled together between or within pores. Additionally, the morphology of nHAp/GEL/Al_2O_3 and pure GEL scaffolds were different in terms of pore size and shape. But the composites nHAp/GEL/TiO_2 and nHAp/GEL/ZrO_2 reveal the same surface morphology.

3.4. TG/DTA analysis

Fig. 5(a) corresponds to the thermo gravimetric analysis (TGA) and differential thermal analysis (DTA) of the calcined powder obtained by the wet chemical procedure. There are two stages of mass loss, the first one is of 3.39% at T_{room}, T, 351.75 °C and the second one is of 0.81% at 738.74 °C, T, 821.48 °C. There is an initial loss due to water evaporation at less than 100 °C. Calcination of the nHAp occurs at *ca.* 600 °C.

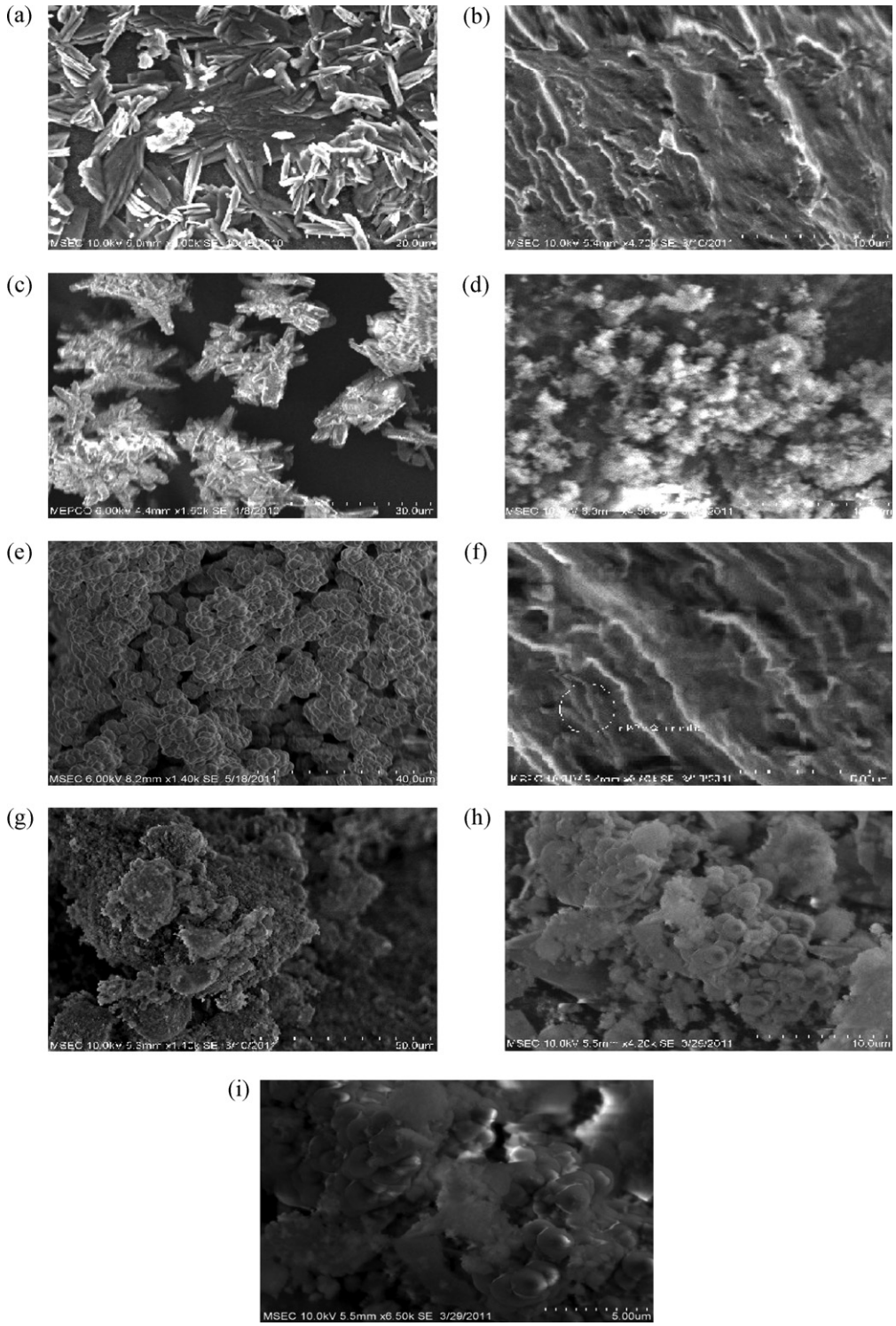

Fig. 4. SEM images of (a) nHAp, (b) GEL, (c) alumina, (d) titania, (e) zirconia, (f) nHAp/GEL, (g) nHAp/GEL/alumina, (h) nHAp/GEL/titania and (i) nHAp/GEL/zirconia.

Over the temperature interval 351.75 °C < T < 821.48 °C there is a very slight slope attributed to the release of gas inside the sample. Exothermic processes, registered at 399.12 °C < T < 807.98 °C, shows the crystallization of nHAp [25]. The small peak located at 1100 °C corresponds to the decomposition of HCO_3. With increasing temperature from 251.24 °C to 1100 °C no peak has been observed, except a weight loss of 11.4%. It is observed at the TGA curve in the temperature range which is assumed to be the result of gradual dehydroxylation of HA powder. This can be explained by reaction Eq. (2) [25].

$$Ca_{10}(PO_4)_6(OH)_2 \rightarrow Ca_{10}(PO_4)_6(OH)_{2-2x}Ox\square_x + xH_2O \quad (2)$$

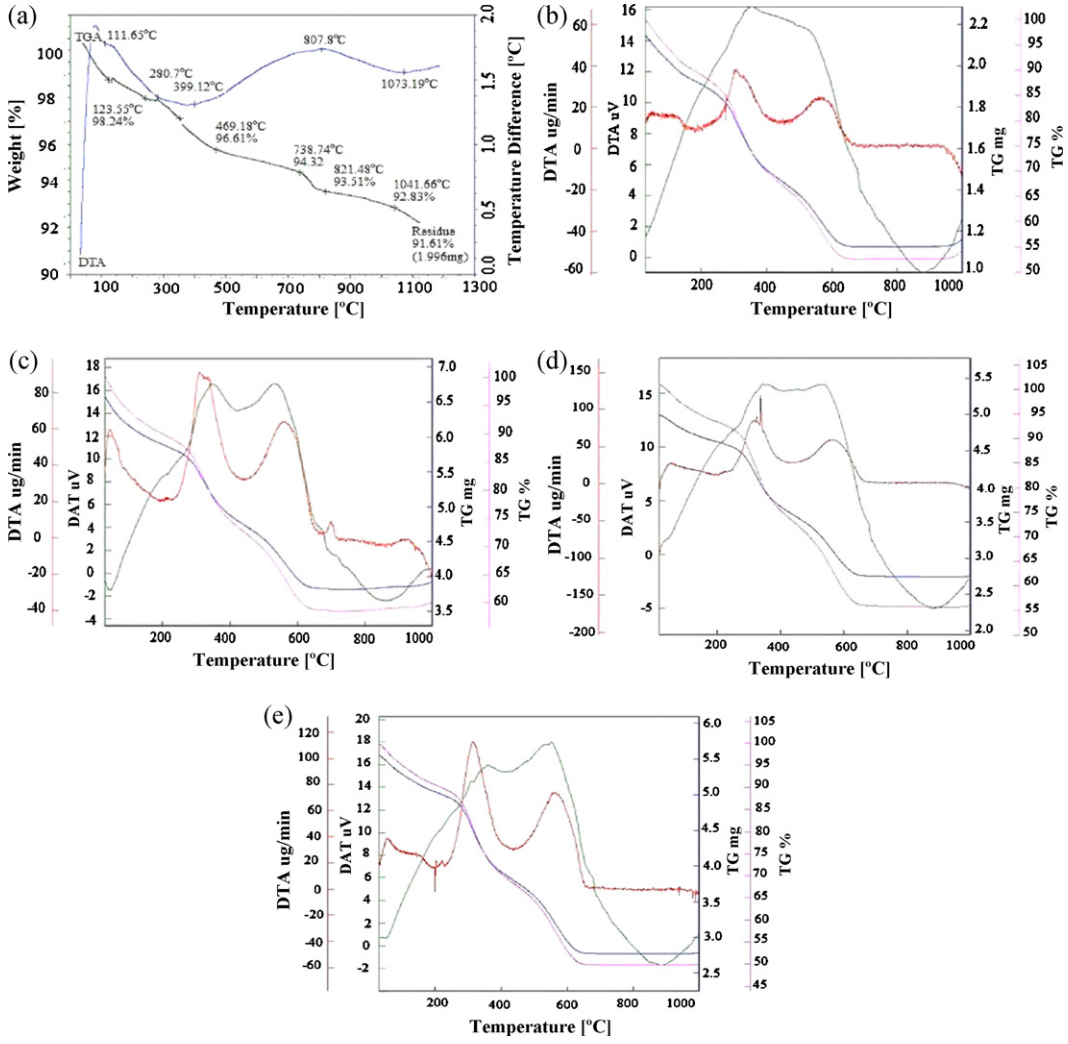

Fig. 5. TG/DTA graph of (a) nHAp, (b) nHAp/GEL, (c) nHAp/GEL/Al_2O_3, (d) nHAp/GEL/TiO_2 and (e) nHAp/GEL/ZrO_2.

From the TG-DTA for nHAp/GEL in Fig. 5(b), an exothermic peak appears at approximately 340 °C, indicating the existence of absorbed water. There are mass losses up to 12% at 190 °C and 18% at 340 °C. The organic components of the composite are dissociated with an increase in the temperature. Carbon dioxide is released from carbonate in the nHAp phase above 800 °C and the crystal lattice water eventually disappears at approximately 980 °C [26]. There are several steps in the decomposition of the organic components in nHAp/GEL, including 350, 510, and 700 °C [27]. This is caused by the decomposition of the GEL molecules. In the nHAp/GEL nanocomposite, four temperature zones of 190 °C, 270 °C, 390 °C and 610 °C typically appear, but other composites also show the same peaks with initial variation in temperature (Fig. 5(b–e)).

The TG/DTA Fig. 5(c) curve shows similar thermal analysis spectra for the nHAp/GEL/Al_2O_3 nanocomposite. There are endothermic peaks between 0 °C and 80 °C and exothermic peak observed 80 °C and 325 °C. This may be due to the evaporation of organic component since it is gelatin. The absorbed water was released as the temperature increased [26]. It shows the mineralization of nHAp phase in the combined matrix of GEL with alumina. The crystal development of nHAp of is very fine, compared to other constituents. The temperature around 450 °C in Fig. 5(b–e) indicates the phase change and/or decomposition. From TG and DTA it shows the decomposition of organics between 290 °C and 600 °C. It was considered that the GEL macromolecules were modified by a small amount of nHAp and alumina that were incorporated into the molecular structure and that the mineralizing clusters of nHAp and additional bioactive ceramic phase interacted with the interpenetrating network structure of the GEL.

TG/DTA data for nHAp/GEL/TiO_2 showed similar results of an exothermic peak at 400 °C and 595 °C correspond to the thermal degradation and pyrolyzation of GEL molecules, followed by distinct endothermic peak of 895 °C (Fig. 5(d)). The peaks 590 °C and 1000 °C are associated with the final thermal degradation of the residual organics. The first exothermic temperature of GEL occurred at 305 °C and 400 °C, thermal degradation of nHAp/GEL/TiO_2 composites began at approximately 200 °C. nHAp/GEL/TiO_2 showed a huge exothermic peak at 395 °C due to the large amount of residual organics which disappeared above 1000 °C [27]. From TG data of nHAp/GEL/TiO_2 (Fig. 5(d)) it was observed 40%

loss in sample mass around of 1000 °C. Another endothermic temperature was located at just below 800 °C, corresponding to the release of carbon dioxide from carbonated apatite. Carbon dioxide is dissolved into the aqueous solution during the preparation reaction and reacted with hydroxyl ions and/or phosphate ions of nHAp. The mineral contents in the synthesized powders can be accessed from TG data (Fig. 5(d)).

The TG/DTA curve of nHAp/GEL/ZrO_2 results (Fig. 5(e)) strongly supports the existence of a chemical bond between nHAp, zirconia and GEL in the composite. Normally GEL loses a large part of its organizing energy through the denaturization in the preparation process. Thermal degradation of GEL molecules corresponds to the micro-disorganization followed by macro-disorganization of helical structures. It is believed that the huge exothermic peak at 360 °C [26] is caused by the decomposition of GEL molecules combined with nHAp nanocrystals. In this sample very tiny nanocrystals are uniformly dispersed in the GEL matrix as shown by SEM analysis (Fig. 4(i)). It is inferred that the nanocrystals having the width of several nanometers are chemically bound with the GEL molecules. That is, this sample has a greater number of organic–inorganic chemical bonds between GEL macromolecules and nHAp phase. The organic–inorganic bond energy was released as a huge amount of exothermic heat at peak 560 °C [28] as shown in Fig. 5(e) for the nHAp/GEL/ZrO_2.

3.5. Porosity

Porosity is an important micro structural feature in most natural and man-made materials and often affects significantly physical properties of these materials such as elastic moduli and yield strength, rupture or ductile strength.

The average porosity of all scaffolds is shown in Fig. 6. The porosity of pure GEL scaffolds (87.2%) decreases by addition of nHAp content in nHAp/GEL scaffold (85.3%). The standard deviation of porosity for the samples is found to be between 0.8165 and 2.2050. The porosity of nHAp/GEL/Al_2O_3 scaffolds of different weight percentage gradually decreases from 84.1% to 79.5% whereas for nHAp/GEL/TiO_2 composites the porosities vary from 82.2% to 77.4%. For nHAp/GEL/ZrO_2 scaffolds it is in between 81% to 74%. The decrease in the porosity upon inclusion of ceramic particles with nHAp/GEL composite may be likely due to the occupation of available space in pores of GEL [22]. The effect of zirconia particles on the porosity is higher than that of alumina and titania particles. It is also inferred from the TG/DTA curve of the nHAp/GEL/ZrO_2 composite that rapid mass loss was observed up to 20% due to particle fragmentation leading to decrease in the development of porosity.

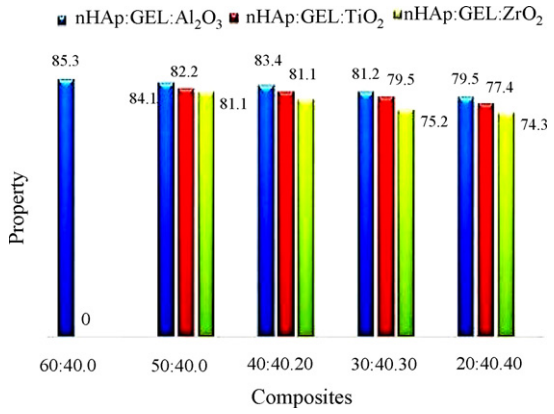

Fig. 6. Porosity content of nHAp/GEL and nHAp/GEL/ceramic scaffolds.

3.6. Mechanical property

3.6.1. Compressive strength and modulus

On early stage, dense forms of bio materials have been used to repair bone defects. For in-growth of bone tissue, porous biomaterials were developed for clinical applications. From dense to porous form of biomaterials was inspired from the cancellous bone structure. To increase mechanical properties, the porous materials of different bio ceramics reinforced nHAp/GEL composites were explored.

The mechanical test was performed on the nHAp, nHAp/GEL, nHAp/GEL/Al_2O_3, nHAp/GEL/TiO_2 and nHAp/GEL/ZrO_2 composite scaffolds (Fig. 7(a–d)). The compressive strength and modulus of nHAp/GEL/Al_2O_3 scaffolds increased with alumina content (Table 2). The nHAp/GEL scaffold prepared using phase inversion techniques had a compressive modulus of 0.11 GPa and it was raised to 0.29 GPa when alumina was introduced as a reinforcing element. The addition of bioinert ceramics into the scaffold improved the mechanical properties (Fig. 8). When the porosities of the scaffolds decreased from approximately 85.3–74.3% (refer Table 2), the compressive strength of the composites gradually increased from 4.87 to 13.15 MPa, and the modulus from 0.11 to 0.79 GPa. The standard deviation of compressive strength and modulus for the samples are assessed between 0.0962–0.3138 and 0.01–0.0573, respectively. Because of high porosity, it is difficult to achieve high compressive strength for porous materials [22]. So it is realized that the compressive strength and modulus decreased with the growth of scaffold's porosity.

Porous materials always have poor mechanical properties. Applications of porous hydroxyapatite in the body have been

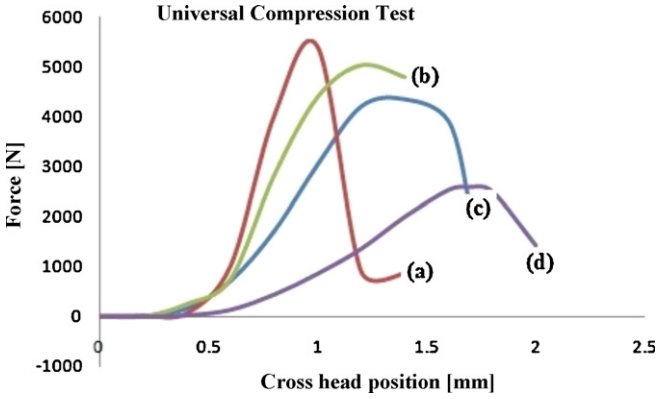

Fig. 7. Compressive strength of nano composites of (a) nHAp:GEL:Al_2O_3 (20:40:40), (b) nHAp:GEL:TiO_2 (20:40:40), (c) nHAp:GEL:ZrO_2 (20:40:40), (d) nHAp:GEL (60:40).

Table 2
Mechanical properties of composite scaffolds.

Mechanical properties	Composite scaffolds											
	nHAp	nHAp/GEL/Al_2O_3					nHAp/GEL/TiO_2				nHAp/GEL/ZrO_2				
		60:40:0	50:40:10	40:40:20	30:40:30	20:40:40	50:40:10	40:40:20	30:40:30	20:40:40	50:40:10	40:40:20	30:40:30	20:40:40
Porosity (%)	70	85.3	84.1	83.4	81.2	79.5	82.2	81.1	79.5	77.4	81.1	78.6	75.2	74.3
Standard deviation	0.8165	0.8178	1.77	1.70	1.0217	0.7982	0.7363	1.3800	0.7761	0.9389	1.06	1.6739	2.2050	1.5577
Compressive strength (MPa)	1.94	4.87	5.43	6.40	8.15	13.1	4.87	5.51	5.92	10.1	6.42	6.61	6.84	9.5
Standard deviation	0.045	0.29	0.3021	0.1224	0.1400	04262	0.1715	0.0962	0.0668	0.5346	0.0698	0.3188	0.0927	0.2654
Compressive modulus (GPa)	0.05	0.11	0.12	0.14	0.29	0.29	0.47	0.47	0.49	0.53	0.61	0.57	0.58	0.79
Standard deviation	0.015	0.052	0034	0.0009	0.056	0.071	0.067	0.019	0.021	0.037	0.098	0.076	0.045	0.074

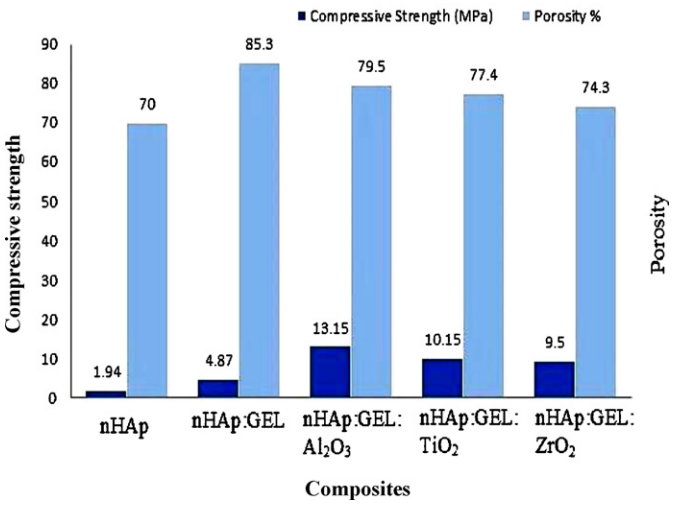

Fig. 8. Effects of ceramic content on the compressive strength and porosity.

limited by their low strength. Numerous techniques have been investigated to retain their useful bioactive properties while providing more suitable mechanical properties for particular applications [29]. The average compressive strength of the cancellous bone is 2–12 MPa [30] and it is 24–43 MPa, 48–80 MPa for the vertebral and femoral bone respectively [31]. For load bearing bone defect applications, synthetic bone graft materials should have suitable mechanical properties, which are at least in the range of cancellous bone.

It was observed that the increase of compressive strength with the decrease of porosity in nHAp/GEL/TiO_2 [22] and nHAp/GEL/ZrO_2 composites also. The compressive strength for nHAp was found as 1.04 MPa. But this was raised to 4.87 MPa when gelatin was added. Still the strength was high up to 13.5 MPa whilst the alumina was introduced as an additional reinforcement in the ratio of 20:40:40. For the same weight ratio, the compressive strengths were found as 10.15 MPa and 9.5 MPa for the nHAp/GEL/TiO_2 and nHAp/GEL/ZrO_2 composites respectively. The composites with zirconia reinforcement showed higher modulus 0.79 GPa when compared with other composites. It can be deduced from the Table 2, the effect of zirconia as a reinforcing element along with nHAp is not much substantial because of the low compressive strength 9.5 MPa even though it is consistent with natural cancellous bone.

3.6.2. Nano hardness

Nanoindenting is another method to characterize the mechanical properties of materials on a very small scale. Features less than 100 nm across, as well as thin films less than 5 nm thick, can be evaluated. Test methods include indentation for comparative and quantitative hardness determination and scratching for evaluation of wear resistance and thin film adhesion. Nanoindentation enables the user to perform indentation test to measure material properties, such as nanoscale hardness and elasticity. Single indentation cycle consists of loading, holding and unloading processes. A whole indentation measurement process may consist of a single cycle,

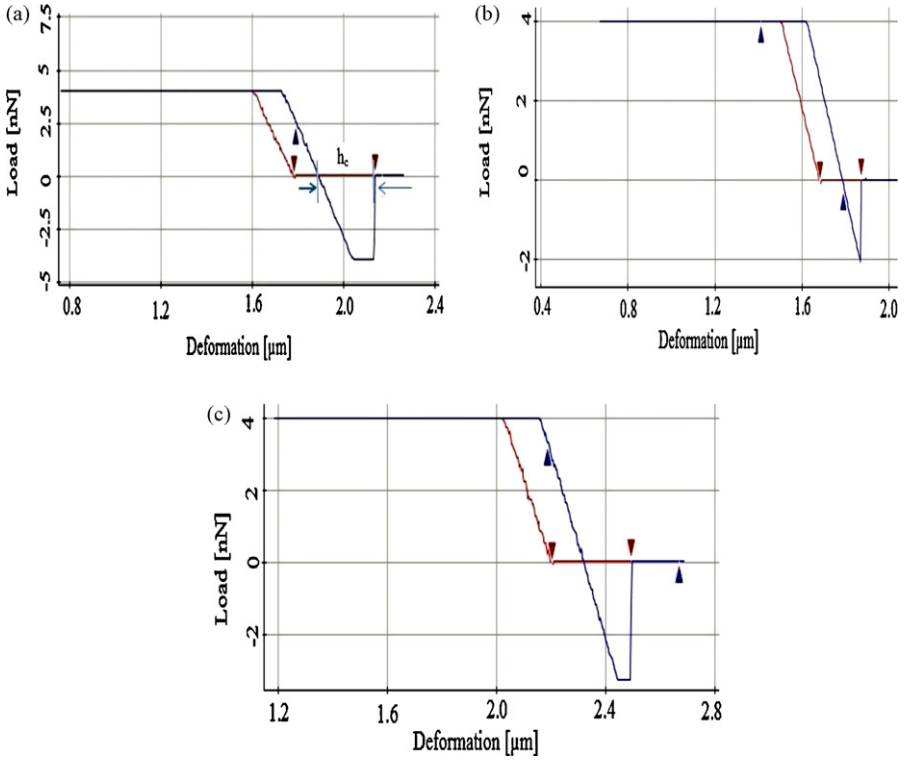

Fig. 9. Representative *F*/*D* curves for (a) nHAp:GEL:Al_2O_3, (b) nHAp:GEL:TiO_2, (c) nHAp:GEL:ZrO_2. (For interpretation of the references to color in this text, the reader is referred to the web version of this article.)

or can be divided into many cycles with gradually increasing loads.

For indentation, the probe is forced into the surface at a selected force. In scratching, the probe is dragged across the sample surface. The scratch is controlled by the parameters like force, rate, length and angle of indentation. Imaging is performed in situ using the probe in intermittent contact AFM. The depth of the indentation is measured from the AFM image to evaluate hardness. A force-displacement curve obtained during indentation also provides indications of the sample material's mechanical properties.

Initially, when the indentation progresses, the force required for indentation increases which is indicated by the red line. After applying the denoted highest load, the tip freely penetrates the material which is shown by the inclined (dotted) blue line following the red line (Fig. 9). Then, the tip is removed gradually from the material. At this instance, again the metal slightly resists the movement of nano indenter depends on material property. The composite powder samples have the different deformation (h_c) value for the load input of 4 nN. This has been verified with four different points in the sample. The *F*–*D* curve is also plotted as shown in Fig. 9(a–c). From these results, the hardness (*H*) can be calculated by using the formula (3) [32]:

$$H = \frac{P}{24.5(h_c)^2} \tag{3}$$

where *P*, maximum applied load; h_c, penetration depth. It is deduced from Table 1 that, increasing bioactive ceramic content produces more amount of secondary matrix and thereby increases hardness. All these facts are also substantiated from various results (SEM and XRD). Fig. 10 shows the relationship between the applied force, penetration depth and nano harness. The alumina reinforced nHAp/GEL composite showed superior nano hardness with not as much of penetration depth. The pure nHAp has little nano hardness with huge penetration depth.

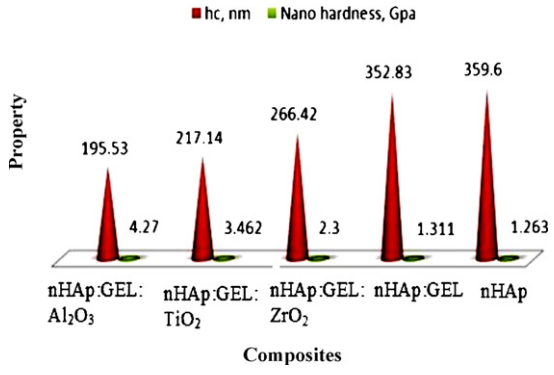

Fig. 10. The relationship between nano hardness h_c and composites.

3.6.3. Vickers hardness and fracture toughness

By far, the most widely used technique in the literature for assessing the fracture toughness directly from indent cracks utilizes the Vickers indenter. This technique was developed to estimate the fracture toughness of ceramic materials by measuring the lengths of cracks emanating from Vickers indents [33,34]. The method has subsequently received much

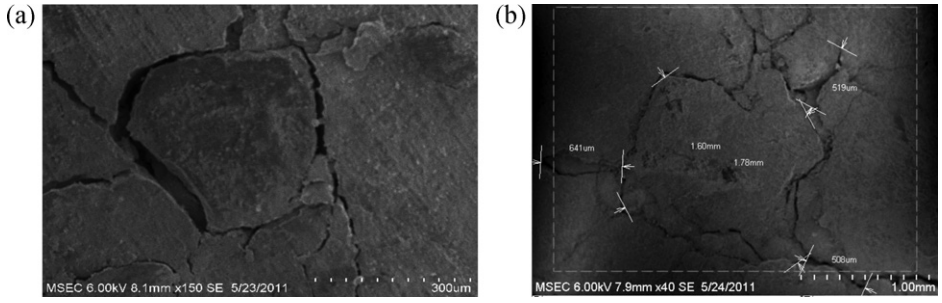

Fig. 11. Representative Vickers indentation obtained on the surface of composite.

recent attention for making measurements of fracture toughness in biomaterials [35]. A later model by Laugier [36] derived a similar expression, with E/H raised to the 2/3 rather than 1/2 power and accordingly a different calibration constant.

In this study, Fracture toughness (K_{IC}) was determined on 1 μm polished samples by an indentation technique as proposed by Laugier. According to the following equation:

$$K_{IC} = 0.015\left[\frac{c-a}{a}\right]\left[\frac{E}{H_v}\right]^{2/3}\left[\frac{P}{(c)^{3/2}}\right] \quad (4)$$

where c is the crack length, a, the half of the diagonal indentation, E, the Young's modulus, H, the hardness, P, the load applied and y is a polynomial function of c/a. Indentations were carried out using a Vickers hardness tester with a pyramid shaped indenter, to a maximum load of 300 N for 10 s using a pyramid shaped diamond indenter. Samples were kept in HBSS until the time of testing and were indented immediately after removal from HBSS to ensure the samples were fully hydrated. Each specimen was indented three times on the positioning of each indentation for each result. The indentation sites were then examined in a scanning electron microscope to provide high-resolution images of the indentations. These indentations were also used to determine hardness using the Eq. (5). Due to the high porosity of the samples, Vickers indentation was difficult.

$$\text{Vickers hardness, } H = 1.8544\frac{P}{d^2} \quad (5)$$

where d is the total length of diagonal indentation.

Fig. 11 shows a pyramid indent in the samples made with a load of 300 N. Initially for the applied load of 100 N, the samples showed no crack developed in the composite surface. Fig. 11 is representative of the other indents and indicates that cracks emanating from the indentation corners and a deep impression due to plastic deformation are evident. In the rare occasion where small cracks were observed in the vicinity of the indent corner as shown in Fig. 11(a and b), difficulties arose deducing whether these cracks were generated during indentation or were associated with pre-existing micro crack damage.

The cracks emanating from the vertices and diagonal of indentations were measured and both K_{IC} and hardness determined. The variation of the fracture toughness results with the compressive modulus may be seen in Table 3. The standard deviation of Vickers hardness and fracture toughness for the samples are calculated between 3.6375–6.3271and 0.0632–0.2765, respectively. No significant changes in the fracture toughness of composite scaffolds were observed as a function of compressive modulus. The maximum fracture toughness value of 6.09 MPa $m^{1/2}$ was obtained for the zirconia composite (nHAp/GEL/ZrO_2: 50/40/10) (Fig. 12(c)) with porosity of about 81.1% whereas the alumina reinforced nHAp/GEL registered 5.59 MPa $m^{1/2}$ as the maximum fracture toughness (Fig. 12(a)). Comparing all the bio ceramic reinforced nHAp/GEL composite scaffolds, the nHAp/GEL/TiO_2 (Fig. 12(b)) showed less fracture toughness than other composites. The behavior of decrease in Vickers hardness caused due to the increase in ceramic concentration. Fracture occurs less frequently in these nano composites especially for TiO_2 and ZrO_2 because of increasing bio inert ceramic content.

Table 3
Comparison of mechanical properties of composite scaffolds.

Mechanical properties	nHAp/GEL/Al_2O_3					nHAp/GEL/TiO_2				nHAp/GEL/ZrO_2			
	60:40:0	50:40:10	40:40:20	30:40:30	20:40:40	50:40:10	40:40:20	30:40:30	20:40:40	50:40:10	40:40:20	30:40:30	20:40:40
Vickers hardness (HVN)	240.7	141.9	250.58	392.85	504.59	177.57	179.42	177.57	214.62	173.63	217.94	220.05	194.78
Standard deviation	6.2311	4.6847	3.6375	6.3271	4.14	5.3251	4.7856	3.8231	6.1963	4.4175	4.8761	3.3387	6.4532
Fracture toughness MPa.$m^{1/2}$	1.55	5.59	5.25	4.57	4.38	2.66	2.03	1.93	1.17	6.09	4.12	3.18	3.18
Standard deviation	0.056	0.072	0.091	0.082	0.07	0.083	0.058	0.049	0.09	0.12	0.094	0.056	0.039

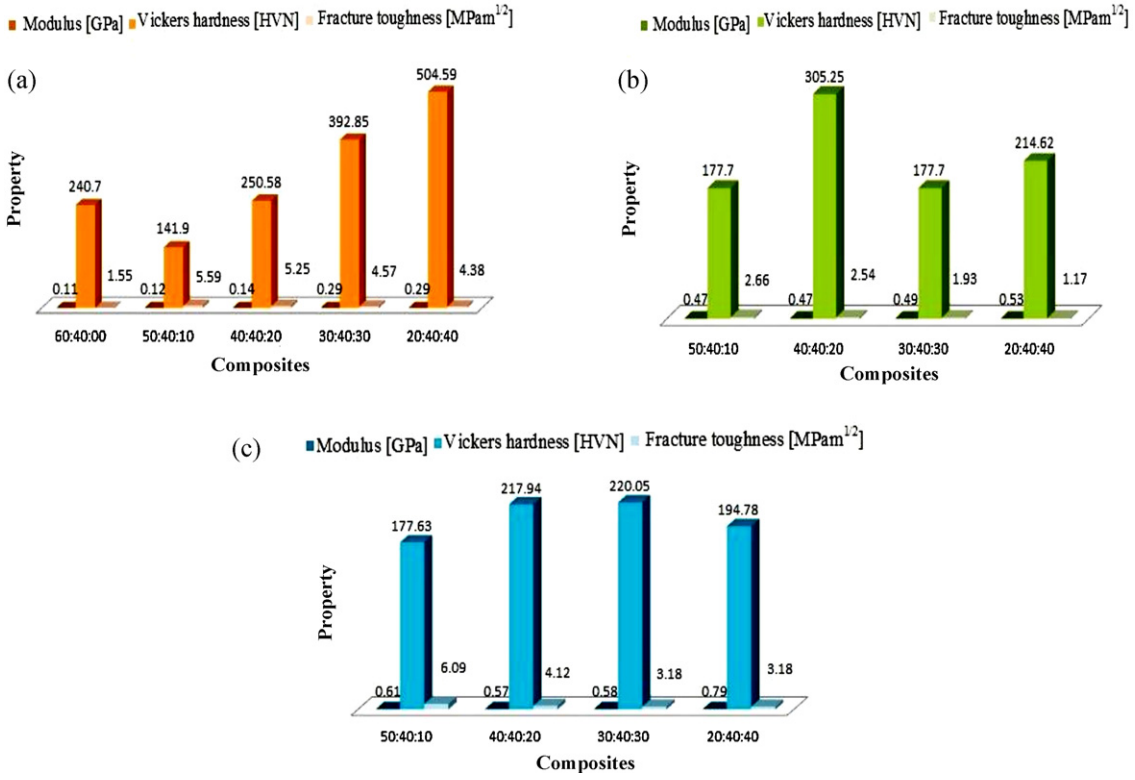

Fig. 12. The graph shown modulus, Vickers hardness, fracture toughness for (a) nHAp/GEL/alumina, (b) nHAp/GEL/titania and (c) nHAp/GEL/zirconia composites.

4. Conclusions

A porous dry product of the nHAp/GEL nanocomposite was obtained. The SEM microstructure showed the dense composite crystallites of nHAp in the GEL matrix. This research investigated new nHAp/GEL/bioinert ceramic composite scaffolds developed using thermally induced phase inversion technique. Novel generations of biodegradable nanocomposites are expected to be biofunctional, and intelligent components. Biopolymer matrix composites have the advantage of being very versatile, allowing for the tailoring of their final properties. The feasible compressive strength was found to have resulted from the organic–inorganic interaction between the nHAp, bioinert ceramic and the organic matrix of the GEL. Nano-sized HAp particles, alumina, titania and zirconia were successfully incorporated into the GEL matrix. The nHAp/GEL/Al_2O_3 composite showed higher compressive strength (13.15 MPa) with porosity of 79.5% than did nHAp/GEL scaffold and modulus increased linearly with increase of ceramic content. The compressive strength of the scaffolds is compared to the compressive strength of the cancellous bone. Even though the obtained values of K_{IC} are less than 6 MPa $m^{1/2}$, they are very well ahead of the fracture toughness of cancellous bone which is 0.1 MPa $m^{1/2}$. Hence it is possible to synthesize the bone grafting materials with enhanced fracture toughness without affecting the microstructure especially for cancellous bone. These outcomes demonstrate that newly synthesized composites perhaps will be better for bone grafting.

References

[1] W.F. Neuman, M.W. Neuman, The Chemical Dynamics of Bone Mineral, The University of Chicago Press, Chicago, 1958.
[2] M.C. Chang, T. Ikoma, M. Kikuchi, J. Tanaka, Preparation of a porous hydroxyapatite/collagen nanocomposite using glutaraldehydeas a cross-linkage agent, J. Mater. Sci. Lett. 20 (2001) 1109–1201.
[3] M.C. Chang, C.-C. Ko, W.H. Douglas, Preparation of hydroxyapatite–GEL nanocomposite, Biomaterials 24 (2003) 2853–2862.
[4] S. Mann, G.A. Ozin, Synthesis of inorganic materials with complex form, Nature 365 (1996) 499–505.
[5] L.H.H. Olde Damink, P.J. Dijkstra, M.J.A. Van Luyn, P.B. VanWachem, P. Nieuwenhuis, J. Feijen, Glutaraldehyde as acrosslinking agent for collagen-based biomaterials, J. Mater. Sci. Mater. Med. 6 (1995) 460–472.
[6] W.B. Brown, J.P. Smith, J.R. Rehr, A.W. Frazier, Octacalcium phosphate and hydroxyapatite, Nature 196 (1962) 1048–1055.
[7] R.A. Young, Biological apatite vs. hydroxyapatite at the atomic level, Clin. Orthop. 113 (1975) 249–260.
[8] A. Ascenzi, G.H. Bell, in: G.H. Bone (Ed.), Bone as a Mechanical Engineering Problem. The Biochemistry and Physiology of Bone, 1, Academic Press, New York, 1972, pp. 311–352.
[9] R. Murugan, S. Ramakrishna, Development of nanocomposites for bone grafting, Compos. Sci. Technol. 65 (2005) 2385–2406.
[10] K. Prabakaran, S. Kannan, S. Rajeswari, Development and characterisation of zirconia and hydroxyapatite composites for orthopaedic applications, Trends Biomater. Artif. Organs 18 (2005) 2.
[11] M. Wang, S. Deb, W. Bonfield, Chemically coupled hydroxyapatite polyethylene composites: processing and characterization, Mater. Lett. 44 (11) (2000) 119–124.
[12] A.C.A. Wan, E. Khor, G.W. Hastings, Preparation of a chitin/apatite composite by in situ precipitation onto porous chitin scaffolds, J. Biomed. Mater. Res. 41 (1998) 541–548.

[13] M. Wang, J. Wang, J. Ni, Developing tricalciumphosphate/polyhydroxybutyrate composite as a new biodegradable material for clinical applications, Biomechanics 192 (2000) 741–744.
[14] H. Li, K.A. Khor, P. Cheang, Titanium dioxide reinforced hydroxyapatite coatings deposited by high velocity oxy-fuel (HVOF) spray, J. Biomater. 24 (2002) 85–91.
[15] A.M. Pietak, J.W. Reid, M.J. Stott, M. Sayer, Silicon substitution in the calcium phosphate bioceramics, Biomaterials 28 (2007) 4023–4033.
[16] Mohan Raja, J. Subha, Fathilah Binti Ali, Sung Hun Ryu, Synthesis of copper nanoparticles by electroreduction process, Mater. Manuf. Process. 23 (8) (2008) 782–785.
[17] D.Jogender Singh, T. Poondi, M. Obbins, MastroPietro, Novel nanomaterials synthesis by laser-liquid-solid interaction, Mater. Manuf. Process. 23 (3) (2008) 228–240.
[18] Z. Stojanovi, L. Veselinovi, S. Markovi, N. Ignjatovi, D. Uskokovi, Hydrothermal synthesis of nanosized pure and cobalt-exchanged hydroxyapatite, Mater. Manuf. Process. 24 (2009) 1096–1103.
[19] C. Kailasanathan, N. Selvakumar, K. Jeyasubramanian, Effect of calcination in synthesis of nano hydroxyapatite for bone grafting, materials and manufacturing processes. (2012), doi:10.1080/10426914.2011.577874.
[20] K. Pal, S. Pal, Development of porous hydroxyapatite scaffolds, Mater. Manuf. Process. 21 (3) (2006) 325–328.
[21] H. Wanga, Y. Li, Y. Zuoa, J. Li, S. Ma, L. Cheng, Biocompatibility and osteogenesis of biomimetic nano-hydroxyapatite/polyamide composite scaffolds for bone tissue engineering, Biomaterials 28 (2007) 3338–3348.
[22] C. Kailasanathan, N. Selvakumar, V. Naidu, Structure and properties of titania reinforced nano-hydroxyapatite/gelatin bio-composites for bone graft materials, Ceram. Int. 38 (1) (2012) 571–579.
[23] M. Ray, S. Ganguly, M. Das, S. Datta, N.R. Bandyopadhyay, S.M. Hossain, Artificial neural network (ANN)-based model for in situ prediction of porosity of nanostructured porous silicon, Mater. Manuf. Process. 24 (1) (2009) 83–87.
[24] E. Nejati, V. Firouzdor, M.B. Eslaminejad, F. Bagheri, Needle-like nano hydroxyapatite/poly(L-lactide acid) composite scaffold for bone tissue engineering application, Mater. Sci. Eng. C 29 (3) (2009) 942–949.
[25] M.G.S. Murray, J. Wang, C.B. Pontoon, P.M. Marquis, An improvement in processing of Hydroxyapatite ceramics, J. Mater. Sci. 30 (1995) 3061–3074.
[26] M. Gelinsky, P.B. Welzel, P. Simon, A. Bernhardt, U. Konig, Porous three-dimensional scaffolds made of mineralized collagen: preparation and properties of a biomimetic nanocomposite material for tissue engineering of bone, Chem. Eng. J. 137 (2008) 84–96.
[27] L.M. Rodriguez-Lorenzo, J.N. Hart, K.A. Gross, Influence of fluorine in the synthesis of apatites. Synthesis of solid solutions of hydroxy-fluoraatite, Biomaterials 24 (2003) 3777–3785.
[28] J. Yan, A. daga, R. Kumar, J.J. Mecholsky, Fracture toughness and work of fracture of hydrated, dehydrated, and avished bone, J. Biomech. 41 (2008) 1929–1936.
[29] X.L. Wang, H.S. Fan, Y.M. Xiao, X.D. Zhang, Fabrication and characterization of porous hydroxy apatite/â-tricalcium phosphate ceramics by microwave sintering, Mater Lett. 60 (4) (2006) 455–458.
[30] L.L. Hench, Biomaterials: a forecast for the future, Biomaterials 19 (1998) 1419–1423.
[31] S. Nagaraja, Microstructural stresses and strains associated with trabecular bone micro damage, Ph.D. thesis, Georgia Institute of Technology (2006) 139.
[32] K.W. Xu, G.L. Hou, B.C. Hendrix, J.W. He, Y. Sun, S. Zheng, A. Bloyce, T. Bell, Prediction of nano indentation hardness profile from a load–displacement curve, J. Mater. Res. 13 (12) (1998) 3519–3526.
[33] B.R. Lawn, A.G. Evans, D.B. Marshall, Elastic/plastic indentation damage in ceramics: the median/radial crack system, J. Am. Ceram. Soc. 63 (9–10) (1980) 574–581.
[34] G.R. Anstis, P. Chantikul, B.R. Lawn, D.B. Marshall, A critical evaluation of indentation techniques for measuring fracture toughness. I. Direct crack measurements, J. Am. Ceram. Soc. 64 (9) (1981) 533–538.
[35] M.A. Lopes, F.J. Monteiro, J.D. Santos, Glass-reinforced hydroxyapatite composites: fracture toughness and hardness dependence on micro structural characteristics, Biomaterials 20 (21) (1999) 2085–2090.
[36] M.T. Laugier, New formula for indentation toughness in ceramics, J. Mater. Sci. Lett. 6 (1987) 355–356.